Exchange anisotropy in the skyrmion host GaV_4S_8

D Ehlers[1], **I Stasinopoulos**[2], **I Kézsmárki**[3], **T Fehér**[3,4], **V Tsurkan**[1,5],
H-A Krug von Nidda[1], **D Grundler**[2,6] **and A Loidl**[1]

[1] Experimentalphysik V, Zentrum für elektronische Korrelationen und Magnetismus, Universität Augsburg, 86135 Augsburg, Germany

[2] Lehrstuhl für Physik funktionaler Schichtsysteme, Technische Universität München, Physik Department, 85748 München, Germany

[3] Department of Physics, Budapest University of Technology and Economics and MTA-BME Lendület Magneto-optical Spectroscopy Research Group, 1111 Budapest, Hungary

[4] MTA-BME Condensed Matter Research Group and MTA-BME Lendület Spintronics Research Group, 1111 Budapest, Hungary

[5] Institute of Applied Physics, Academy of Sciences of Moldova, MD 2028, Chisinau, Republica Moldova

[6] Laboratory of Nanoscale Magnetic Materials and Magnonics (LMGN), Institute of Materials (IMX), École Polytechnique Fédérale de Lausanne (EPFL), 1015 Lausanne, Switzerland

E-mail: Dieter.Ehlers@physik.uni-augsburg.de

Abstract

Using ferromagnetic resonance spectroscopy at 34 GHz we explored the magnetic anisotropy of single-crystalline GaV_4S_8 in the field-polarized magnetic state. We describe the data in terms of an easy-axis type uniaxial anisotropy with an anisotropy constant $K_1 = 1.6 \cdot 10^5$ erg cm^{-3} at 2 K, corresponding to a relative exchange anisotropy $\Delta J/J \approx 5\%$, and about $1.0 \cdot 10^5$ erg cm^{-3} near 11 K, i.e. at temperatures where the skyrmion-lattice phase was recently discovered. The relatively large value of K_1 explains the confinement of the skyrmion tubes to the $\langle 1\,1\,1 \rangle$ easy axes. A distinct set of resonances in the spectra is attributed to the co-existence of different rhombohedral domains. Complementary broadband spectroscopy demonstrates that non-collinear spin states may sensitively be detected by electron spin resonance techniques.

1. Introduction

Beyond magnetic materials with spinel structure, which receive high interest due to their complex magnetic phase diagrams, recently lacunar spinels AM_4X_8 (A = Ga, Ge; M = Mo, V, Nb, Ta; X = S, Se) gained considerable attention due to a variety of correlation phenomena manifested in their transport properties such as superconductivity under pressure in $GaNb_4Se_8$ and $GaTa_4Se_8$ [1], 4d-heavy-fermion behaviour in $GaMo_4X_8$ [2, 3] or electric-field induced resistive switching in several of these Mott insulators [4, 5]. The main reason for such peculiarities is the presence of weakly linked tetrahedral metal clusters M_4X_4 with little orbital overlap between each other. Magnetic properties then have basically to be understood in terms of cluster-internal orbital, charge and spin degrees of freedom. Such a description has also been applied to the multiferroic and strongly magnetoelectric GeV_4S_8 [6]. Moreover long-range distortions of the high-temperature face-centred cubic structure are common in lacunar spinels, influencing their magnetic and electronic properties [7–9].

Among these systems, GaV_4S_8 with primarily ferromagnetic interactions and magnetic ordering at the Curie

1

temperature $T_C = 13$ K recently has been demonstrated to host a skyrmion lattice at temperatures $9 \leqslant T \leqslant 13$ K and for magnetic fields $H \leqslant 1500$ Oe [10]. A magnetic skyrmion is a whirl-like object of spins, characterized by a quantized nonzero topological winding number. This stable object can be manipulated by spin currents or magnons in possible future spintronic memory devices [11–13]. In bulk materials, skyrmions crystallize in hexagonal periodic arrangements, the skyrmion lattices. Depending on the underlying crystal symmetry, two different kinds of skyrmions may be realized: on approaching the skyrmion core from the periphery, the spins can either rotate tangentially, i.e. they are perpendicular to the radius vector, or radially, where the spins have a component towards the core [14]. In the context of a description of skyrmions as domain walls, the former case is named a Bloch-type skyrmion, as observed in most of the so-far known skyrmion hosts, like MnSi [15, 16], Cu_2OSeO_3 [17–19] or $Fe_{1-x}Co_xSi$ [20]. On the other hand, until now GaV_4S_8 is the only known bulk material hosting Néel-type skyrmions.

In this lacunar spinel, the molecular V_4S_4 clusters carry one unpaired electron with an effective spin $S = 1/2$, which is explained by the molecular orbital scheme of the clusters [7]. In addition, GaV_4S_8 is known to undergo a Jahn–Teller transition at $T_s = 44$ K, where the symmetry is lowered from non-centrosymmetric cubic (space group $F\bar{4}3m$) to rhombohedral ($R3m$) with the axis of distortion along one of the four possible $\langle 1\,1\,1 \rangle$ directions. This leads to a lamellar multi-domain structure of GaV_4S_8 single crystals in the low-temperature rhombohedral state. The resulting magnetic phase diagram below 13 K has been explained based on the identification of the axes of distortion with the uniaxial magnetic anisotropy axes [10]. It contains cycloidal and skyrmion-lattice phases, embedded in the ferromagnetic state. Competing magnetic interactions, namely the Zeeman interaction, antisymmetric and symmetric anisotropic exchange interactions modulate the spin structure as long as the external field does not govern the hierarchy of energies. Additionally, the onset of ferroelectricity was observed upon the Jahn–Teller transition of GaV_4S_8 [21–23]. This compound represents a new type of improper ferroelectrics where ferroelectricity is induced by the Jahn–Teller effect due to the lack of spatial inversion in the high-temperature cubic phase [24]. In contrast to proper ferroelectrics, this mechanism of ferroelectricity requires a partially filled d-shell, hence, it allows for the emergence of magnetism. Indeed, GaV_4S_8 becomes multiferroic below $T_C = 13$ K.

Recently, a broadband electron spin resonace (ESR) study was carried out on GaV_4S_8 at 11 K to explore the dynamic properties of the skyrmion lattice and the cycloidal phase [25]. The dynamics suggested a dominant role of the magnetic anisotropy that, however, was not studied in detail. Here, we make use of angular and temperature dependent ESR to quantify the magnetic anisotropy. This is of key importance to understand the magnetic phases in skyrmion-host materials with axial symmetry. More specifically, in GaV_4S_8 the axial anisotropy originating from the rhombohedral crystal structure was claimed to be responsible for the orientational confinement of the skyrmion cores. In strong contrast to the skyrmions found in cubic helimagnets, in this compound the skyrmion cores do not co-align with the external magnetic field but keep parallel with the rhombohedral axis [10]. Due to the dominance of the axial magnetic anisotropy over the Zeeman energy in the field range where the skyrmion-lattice state exists, the phase transitions between the cycloidal, skyrmion-lattice and ferromagnetic states were found to be solely driven by the magnetic field component parallel to the rhombohedral axis [10, 26]. In this work, we present a study of fixed-frequency ESR in the field-polarized ferromagnetic phase aiming at the direct experimental determination of the anisotropy constant and we also address to broadband ESR results to corroborate the validity of our analysis for arbitrary frequency.

2. Methods

2.1. Crystal growth

GaV_4S_8 polycrystals were prepared by solid-state synthesis from the high-purity elements Ga (99.9999%), V (99.5%) and S (99.999%). Three repeated synthesis cycles were necessary to reach the required homogeneity of the material as checked by x-ray powder diffraction. The polycrystals were used for the growth of single crystals by means of chemical transport reaction in evacuated quartz ampoules. The crystal-growth temperature was kept between 800 °C and 850 °C, and iodine was taken as transport agent. For the measurements in this study, we have chosen as-grown truncated pyramids in the $(0\,0\,1)$ plane with a diameter of 0.5 mm or prepared as platelets in the $(\bar{1}\,1\,0)$ plane with a diameter of 1 mm.

2.2. ESR techniques

2.2.1. Fixed-frequency ESR. Continuous-wave ESR was performed at a frequency of $\nu = 34$ GHz (Q-band). A Bruker ELEXSYS E500 spectrometer was used and the resonator was a cylindrical Bruker ER 920 cavity. A helium gas-flow cryostat allowed a temperature stability of 0.1 K. To measure the angular dependence in the naturally grown $(0\,0\,1)$ plane the samples were mounted with their growth plane perpendicular to the rotation axis of a goniometer. Rotations in the $(\bar{1}\,1\,0)$ plane were performed by mounting a sample in $(0\,0\,1)$ geometry with this latter plane tilted away from the goniometer axis by 45°, with an error of 5°. The external field H was swept up to 1.8 T. The spectra shown in this work are the first derivative of the absorbed microwave power, owing to the use of lock-in technique with field modulation.

2.2.2. Broadband ESR. Electron spin resonance with variable frequency was measured by putting the sample, inside a croygenic chamber, onto a coplanar waveguide (CPW) consisting of a central signal line and two adjacent ground lines connected to the ports of an Agilent PNA N5222A vector network analyzer via microwave tips and semi-rigid high-frequency cables [27]. The microwave frequency ν was swept between 10 MHz and 26.5 GHz. We display $\Delta|S_{12}(\nu)| = |S_{12}(\nu)| - |S_{12}^{\mathrm{ref}}(\nu)|$, where S_{12} is the scattering parameter measured on the CPW in transmission
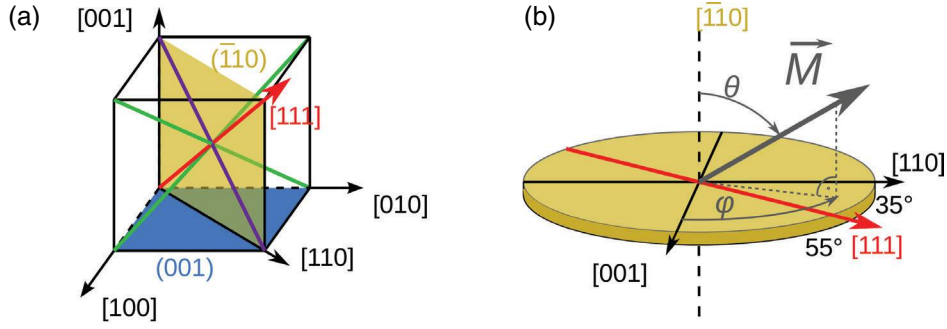
Figure 1. (a) Sketch of the two planes $(\bar{1}\,1\,0)$ and $(0\,0\,1)$ within the pseudocubic crystal structure of GaV_4S_8, together with high-symmetry $\langle 1\,0\,0\rangle$, $\langle 1\,1\,0\rangle$ and $\langle 1\,1\,1\rangle$ crystal directions. (b) Illustration of angles and directions in case of a disk-like sample in $(\bar{1}\,1\,0)$ geometry. In this plane the two angles $35°$ and $55°$ spanned by the high-symmetry directions are characteristic. The orientation of the magnetization vector $\vec{M}$ is defined by the angles θ and φ.

configuration. In order to increase the signal-to-noise ratio, we subtracted a reference spectrum $|S_{12}^{\mathrm{ref}}(\nu)|$ taken at $H = 20$ kOe, where the magnetic resonances lie outside the accessible frequency range.

2.3. Anisotropy simulations

The anisotropy of the resonance fields in Q-band angular dependence is simulated by means of the Smit-Suhl formula [28]

$$\left(\frac{\omega}{\gamma}\right)^2 = \frac{1}{M^2 \sin^2 \theta_0}\left[\frac{\partial^2 F}{\partial \theta^2}\frac{\partial^2 F}{\partial \varphi^2} - \left(\frac{\partial^2 F}{\partial \theta \partial \varphi}\right)^2\right]. \quad (1)$$

Here $\omega = 2\pi \cdot 34$ GHz is the angular microwave frequency, $\gamma = g\mu_B/\hbar$ the gyromagnetic ratio and M the magnitude of the magnetization. The anisotropy is contained as the second derivatives of the magnetic free energy density F with respect to the polar angle θ and the azimuthal angle φ of the magnetization vector $\vec{M}$ in a spherical coordinate system. For a sample rotation in the $(\bar{1}\,1\,0)$ plane we choose this framework such that the polar axis (z-axis) coincides with the axis of rotation and that $\theta = 90°$ and $\varphi = 0°$ in case of $\vec{M}\|[0\,0\,1]$ (x-axis). Figure 1 illustrates relationships between the crystal axes, the magnetization vector and their angles. Rotations in $(0\,0\,1)$ geometry analogously define $\theta = 90°$ and $\varphi = 0°$ for $\vec{M}\|[1\,0\,0]$. In (1), θ_0 denotes the equilibrium value of θ. The free energy density

$$F = F_Z + F_{\mathrm{dem}} + F_{\mathrm{an}}$$

consists of the Zeeman energy $F_Z = -\vec{M} \cdot \vec{H}$, where the external field enters allowing us to determine the resonance field H_{res}, the demagnetization energy $F_{\mathrm{dem}} = \frac{1}{2}N_{\mathrm{eff}}M^2\cos^2\theta$, where $N_{\mathrm{eff}} = N_z - N_x$ is the effective demagnetization factor in ESR experiments, as well as the magnetocrystalline anisotropy energy F_{an}. The demagnetization factor is computed [29] under the approximation of a spheroid-like sample shape with a ratio v between diameter and thickness. The resulting error in the calculation is small owing to the small magnetization ($M = 38$ Oe at low temperatures). The

magnetocrystalline anisotropy is assumed to be uniaxial in the four rhombohedral domains with four different anisotropy axes along the $\langle 1\,1\,1\rangle$ axes of the pseudocubic system. Consequently, four different resonance fields are computed in general. The contributions $F_{\mathrm{an}}^{(i)}$ of uniaxial anisotropy energy read

$$F_{\mathrm{an}}^{(i)} = K_1 \sin^2 \beta_i + K_2 \sin^4 \beta_i + K_3 \sin^6 \beta_i,$$

where $i = 1..4$ denotes the respective rhombohedral domain. The three anisotropy constants K_1 to K_3 are assumed to be equal for the different domains. The angles β_i are spanned by the magnetization $\vec{M}$ and the respective $\langle 1\,1\,1\rangle$ direction. The Smit-Suhl formula is solved self-consistently together with the minimization problem for the free energy which provides the respective equilibrium position (θ_0, φ_0) of $\vec{M}$. The obtained resonance fields $H_{\mathrm{res}}^{(i)}$ are calculated as a function of the azimuthal angle φ_H of the external field. Fit parameters, in particular the anisotropy constants, are adjusted to minimize least squares between calculated and experimental data. The magnetization data at different temperatures are taken from independent magnetometry measurements on a Quantum Design MPMS XL SQUID magnetometer.

Neglecting the demagnetization term and higher order anisotropy terms in (1) the resonance field can be explicitly written as

$$H_{\mathrm{res}}^{\|} = \frac{\omega}{\gamma} - 2\frac{K_1}{M} \quad (2)$$

in case of the external field being parallel to the easy axis and as

$$H_{\mathrm{res}}^{\perp} = \frac{K_1}{M} + \sqrt{\left(\frac{K_1}{M}\right)^2 + \left(\frac{\omega}{\gamma}\right)^2}, \quad (3)$$

when the field lies within the hard plane. In these two cases the magnetization keeps parallel to the external field. Note that for the $[0\,0\,1]$ direction the magnetization is not parallel to the external field, because we deal with uniaxial anisotropy and not with a simple cubic anisotropy. Assuming a fully aligned magnetization along $[0\,0\,1]$ would result in

$$H_{\text{res}}^{[0\,0\,1]} = \sqrt{\left(\frac{\omega}{\gamma}\right)^2 + \frac{4}{9}\left(\frac{K_1}{M}\right)^2}. \tag{4}$$

Below we will show that this expression strongly overestimates the resonance field along [0 0 1].

For a description of broadband ESR data, (1) is solved for ω and the external field is an independent parameter. The energy minimization for $\vec{M}$ then only needs to be performed once. The resonance frequencies for the above special cases follow directly from (2)–(4).

3. Results and discussion

3.1. Q-band ESR

Three spectra obtained at temperature of $T = 5\,\text{K}$ are shown in figure 2, where the field points along the [0 0 1], [1 1 1] and [1 1 0] axes, which are the cubic principal directions. As before, the Miller indices refer to the pseudocubic structure. Depending on the field orientation, the spectra can be well reproduced by fits with a number of first derivatives of Lorentzian-shaped lines, shown as the red curves. The expression for the absorbed microwave power of a single resonance is

$$P(H) = \frac{I[\Delta H + \alpha(H - H_{\text{res}})]}{(H - H_{\text{res}})^2 + \Delta H^2}, \tag{5}$$

where setting $\alpha = 0$ for the analysis of the Q-band ESR means a conventional symmetric Lorentzian line. I is proportional to the integrated intensity and ΔH is the linewidth, which generally lies in the range between 300 and 800 Oe. The number of fitted lines varies between two and seven, depending on the respective angle φ_H.

Figure 3 presents the resulting resonance fields (symbols) as a function of the angle φ_H between the static field and the pseudocubic [0 0 1] direction for a rotation within the ($\bar{1}$ 1 0) plane (figure 1). We identify the following characteristic angular dependencies. At first, one curve (red) exhibits its minimum and maximum fields of $H_{\text{res}} \approx 6\,\text{kOe}$ and 18 kOe at the angles 55° and 145°, respectively. A second curve (violet) shows the same behaviour, but is mirrored at $\varphi_H = 90°$ with respect to the first one. For these two curves a splitting into subcomponents (open/closed symbols) is observed at certain angular ranges. A third curve can be followed, with its maximum of 18 kOe at $\varphi_H = 90°$. Its minimum, however, is no longer a single resonance line, but a set of subcomponents (green symbols) with resonance fields ranging between 9 kOe and 12.5 kOe. This splitting into subcomponents is absent for $\varphi_H \approx 90°$, but most pronounced close to $\varphi_H = 0°$. As will be shown below, splittings into subcomponents are secondary effects compared to the aforementioned distinction of three principal curves.

A main finding from figure 3 is the existence of three symmetric angles at 0°, 55° and 90°. Figure 1 allows to identify the angles as belonging to the pseudocubic [0 0 1], [1 1 1] and [1 1 0] directions, respectively, as is illustrated by vertical dashed lines in figure 3. As a consequence, from the fact that
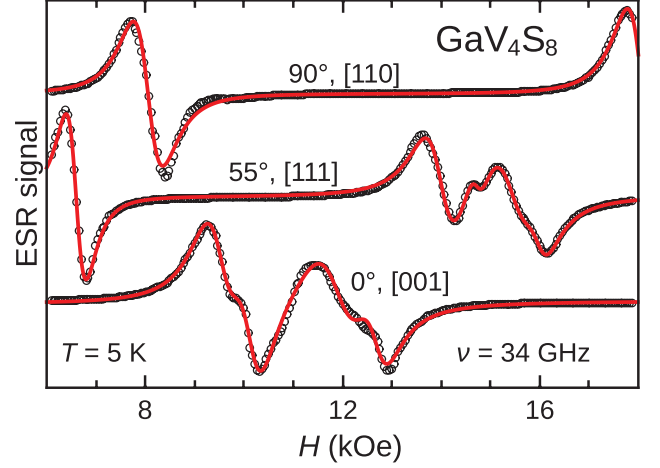

Figure 2. Open circles: Three ESR spectra for a GaV_4S_8 single crystal taken in the three cubic principal directions [0 0 1], [1 1 1], [1 1 0], corresponding to the angles $\varphi_H = 0°, 55°, 90°$. Solid lines: fits by a set of Lorentzian derivatives. In the uppermost spectrum the apparative field limit of 18 kOe still allows for a quantitative analysis of the high-field resonance.

an overall minimal resonance field is reached by one of the lines in the [1 1 1] direction, figure 3 demonstrates easy-axis anisotropy in GaV_4S_8, as has previously been anticipated [10] and supported by band structure calculations [24].

The number of three main resonance components is easily understood when considering the domain geometry: for a rotation with the external field in the ($\bar{1}$ 1 0) plane, two domains with their easy axes within this plane can be distinguished (red and violet symbols) as well as two geometrically and energetically equivalent rhombohedral domains with easy axes out of plane (green symbols). Considering the correspondence of colours between the solid lines in figure 3 and space diagonals in figure 1(a) we can assign the resonances: the curve which has a maximum for $\vec{H} \| [1\,1\,2]$ (i.e. at 35°) and a minimum for $\vec{H} \| [1\,1\,\bar{1}]$ (at 125°) comes from the structural domain whose easy axis is the $[1\,1\,\bar{1}]$ direction. Similarly, the curve which has a maximum for $\vec{H} \| [1\,1\,\bar{2}]$ (at 145°) and a minimum for $\vec{H} \| [1\,1\,1]$ (at 55°) belongs to the structural domain whose easy axis is the [1 1 1] direction. The resonances which have a common maximum for $\vec{H} \| [1\,1\,0]$ (at 90°) and a minimum for $\vec{H} \| [0\,0\,1]$ (at 0°) result from the domains with easy axes along the $[1\,\bar{1}\,1]$ and $[\bar{1}\,1\,1]$ axes.

A least squares fit as described in section 2.3 has been applied to the resonance component indicated by the red solid circles in figure 3. The result is shown as the red solid line. Free parameters in this procedure are the Landé g-factor and the anisotropy constant K_1; the other parameters (ω, M and geometric ratio v) have been taken from independent measurements, see section 2.3. We get $g = 1.74$ and $K_1 = 135 \cdot 10^3$ erg cm^{-3}, whereas K_2 and K_3 are less than one percent of K_1 and, thus, were set to zero for this fit. The agreement between theory and experiment quantitatively documents that uniaxial anisotropy governs the local field in the field polarized ferromagnetic state, here probed by ESR. The obtained parameters are subsequently applied to the remaining domains, providing us with the violet and the green solid lines, which, especially
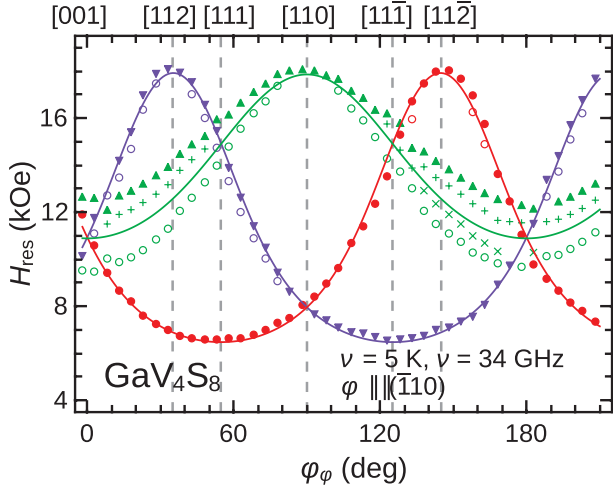
[001] [112] [111] [110] [11$\bar{1}$] [11$\bar{2}$]

Figure 3. Symbols: Angular dependence of the resonance fields as extracted from the Lorentzian fits of the spectra for a rotation in the ($\bar{1}\,1\,0$) plane. Different symbol shapes and colours represent different curves of resonance fields which can be followed by eye. Red solid line: fit of the uniaxial model of anisotropy to the red symbols. Violet and green solid lines are simulated with the same parameters. The colours are chosen corresponding to the cubic space diagonals in figure 1, indicating the respective easy axes. Vertical dashed lines illustrate symmetric cubic directions.

in the case of the violet curve, yield satisfying agreements with the corresponding experimental data of the same colour, too.

Inserting the above values, the analytical expressions (2) and (3) give us a minimal resonance field of 6.74 kOe and a maximal one of 18.1 kOe. They are about 0.2 kOe off from the simulation values, so that the demagnetization effect may be considered rather negligible. On the other hand, (4) yields a resonance field of 14.2 kOe, which is far from the simulated 10.9 kOe. As mentioned above, the reason for this large shift is that the internal anisotropy fields tilt the magnetization direction away from a parallel alignment to the external field and the simulation takes this into account. This consideration conversely lets us estimate the angular tilting of the magnetization as 12° for $\vec{H}\|[0\,0\,1]$.

The secondary splitting of the upper resonance component along the $\langle 1\,0\,0\rangle$ directions amounts to approximately 3 kOe for the sample measured in figure 3. Another sample (not shown here), prepared in the same ($\bar{1}\,1\,0$) geometry, where an angular dependent measurement equivalent to figure 3 has been performed, shows a splitting in the range of 1 kOe only, and otherwise the same magnetic anisotropy. Considering this, the secondary splitting can be regarded as a sample-dependent effect, being remarkably large for the sample shown. Since the magnetic anisotropy is governed by the structural rhombohedral distortion of domains, this result possibly indicates a distribution of the local strain. It may arise from the lamellar domain structure developing on a microscopic scale as identified independently in [10]. The different domains cannot independently undergo the preferred rhombohedral distortion and small tiltings of the distortion axes lift the equivalence of domains. However, magnetic domain-domain interactions due to effective exchange interactions or magnetoelastic couplings cannot be excluded for a complete explanation.

Angular scans within the as-grown ($0\,0\,1$) plane have been performed on another sample in the temperature range from 2 to 15 K. Three examples are given in figure 4, which depicts the resonance fields at 2 K, 10 K and 15 K from such rotations. Two main components of resonances are visible, with minima at $\varphi_H = 45°$ and 135°, respectively. They arise from two pairs of domains as in this geometry always two rhombohedral axes span the same angle with the external field and consequently are expected to give the same resonance field. Even though the ($0\,0\,1$) plane lacks the symmetric pseudocubic $\langle 1\,1\,1\rangle$ directions and consequently gives less information than a rotation in a ($\bar{1}\,1\,0$) plane, the closed yellow data points (triangles) are again successfully described in terms of a K_1-only uniaxial anisotropy. The blue solid lines, which apply the parameters of the yellow lines to the other pair of domains, here again describe the blue data points (circles) sufficiently well. Like before, K_2 and K_3 turned out to be unnecessary to reproduce the data. The three frames in figure 4 demonstrate that the magnetocrystalline anisotropy gets reduced with increasing temperature. Generally, ESR spectra in GaV$_4$S$_8$ could be resolved up to 30 K, but the anisotropy rapidly decreased around the temperature of the magnetic order at $T_C = 13$ K. Note that in this sample, too, a secondary splitting of up to 1.5 kOe is observed, which is seen as the open and closed symbols in figure 4. We exclude sample misalignment as the origin of this splitting, since this would lead to subcomponents crossing at a certain angle. The fact that the yellow, fitted curve of uniaxial anisotropy best matches the closed yellow triangles (lower subcomponent) over the whole angular range excludes such a scenario and points to the same mechanism of secondary splitting as in the case of $\vec{H}$ rotated in the ($\bar{1}\,1\,0$) plane.

With these angular dependent ESR measurements in the ($0\,0\,1$) plane performed in a temperature range covering the whole ferromagnetic phase, the temperature evolution of K_1 as obtained from uniaxial anisotropy fits is documented in figure 5. At low temperatures we find $K_1 \approx 160 \cdot 10^3\,\text{erg}\,\text{cm}^{-3}$. The value drops to $70 \cdot 10^3\,\text{erg}\,\text{cm}^{-3}$ at the transition temperature $T_C = 13\,\text{K}$. The inset, where K_1 is plotted against the squared magnetization, clearly proves that the anisotropy constant is proportional to M^2. Such a behaviour is consistent with the fact that the magnetocrystalline aniosotropy originates from an anisotropy ΔJ of the exchange coupling parameter J. Our low-temperature value of K_1 corresponds to $\Delta J = 0.15\,\text{K}$ and supports an earlier calculation based on magnetization data [10]. The value of K_1 in GaV$_4$S$_8$ may be considered rather typical in comparison to other ferro- or ferrimagnetic thiospinels [30, 31]. In the anisotropy analyses of figures 4 and 5, the values of ω, M and ν are again taken from independent measurements, while the g-value as the second free parameter varies between 1.76 and 1.83.

3.2. Broadband ESR

ESR spectra obtained by the frequency-sweep setup at $T = 8\,\text{K}$ with $\vec{H}\|[1\,1\,1]$ are displayed in figure 6. Resonances now show up as minima in the transmission signal $\Delta|S_{12}(\nu)|$. It is seen that a low-frequency resonance persists up to 1000 Oe, whereas a high-frequency resonance strengthens with
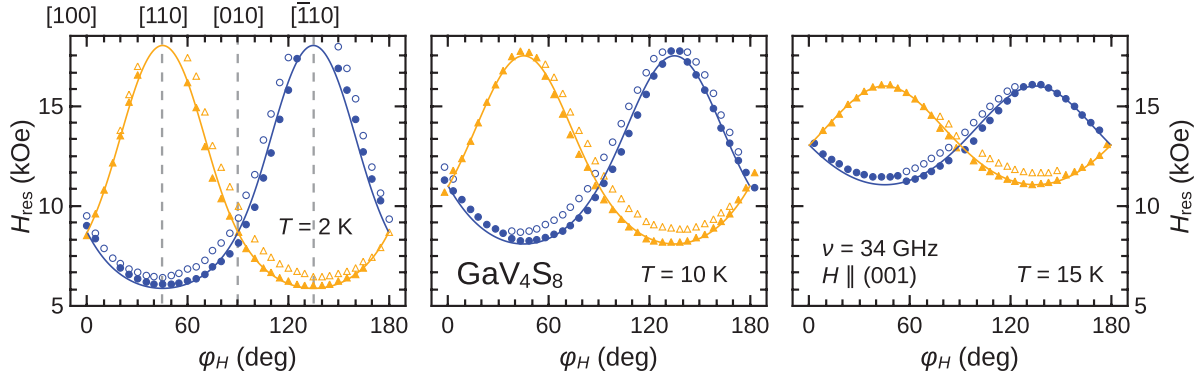
Figure 4. Angular dependences of the resonance fields (symbols) in GaV_4S_8 at $T = 2\,\text{K}$, $10\,\text{K}$ and $15\,\text{K}$ for a rotation within the $(0\,0\,1)$ plane with φ_H as the angle between external field and the $[0\,0\,1]$ direction. Different symbols and colours represent different curves of resonance fields. Solid lines are fits taking into account uniaxial anisotropy.

increasing field. Measured resonances in the cavity experiments were well described by symmetric Lorentzian lines. This is not the case for the broadband ESR spectra. For the fitted curves (red lines) in figure 2, fields H in (5) are replaced by frequencies ν and we considered $\alpha \neq 0$, thereby including an antisymmetric contribution. Depending on the respective spectrum and line, α is found to lie between -0.9 and 0.9, but mostly $|\alpha| \leqslant 0.3$. An asymmetric absorption line is often taken as a limiting case for the ESR absorption in metals [32, 33]. In the present case we do not consider an intrinsic property for $\alpha \neq 0$. Instead, we attribute the antisymmetric contribution to the CPW setup, which can admix a dispersion component (antisymmetric) into the absorption part (symmetric) of the dynamic susceptibility. Moreover, following [27], a slight asymmetry of the spectra may result from a non-resonant background signal emerging from the difference technique. Linewidths are typically $\Delta\nu \approx 1\,\text{GHz}$ and an error of $0.3\Delta\nu$ for ν_{res} may be estimated. Resonance frequencies extracted from the spectra at $T = 8\,\text{K}$ and $18\,\text{K}$ are presented in figure 7, where the field has been decreased from 10 to 0 kOe during the measurement. At $18\,\text{K}$, magnetic anisotropy is negligible and the resonance frequency is proportional to the external field over the covered field range. A linear regression yields a slope $2.55\,\text{GHz}\,\text{kOe}^{-1}$, corresponding to $g = 1.82$. This is in excellent agreement with the value obtained from the anisotropy simulations in section 3.1.

For $T = 8\,\text{K}$ we identify a branch (topmost) with a steep slope $d\nu_{\text{res}}/dH$. This branch is attributed to the domain for which the easy axis is parallel to $\vec{H}$. In this case, the anisotropy field adds to the applied field in the equation of motion and ν_{res} is large. The extrapolation of this branch to 34 GHz yields a resonance field of 6.6 kOe in the Q-band, which matches exactly the value at $\varphi_H = 55°$ in figure 3. The other branches with ν_{res} between 18 and 26 GHz for $H > 1$ kOe reflect the other domains, for which the easy axes span an angle of $71°$ with $\vec{H}$. For these three domains, the magnetization is close to the magnetic hard plane and consequently the resonance frequencies are below the steep branch. Although in the orientation the resonance frequency is expected to be equal for these three domains, we observe a splitting into three subcomponents. Their extrapolation to 15 kOe–17 kOe again
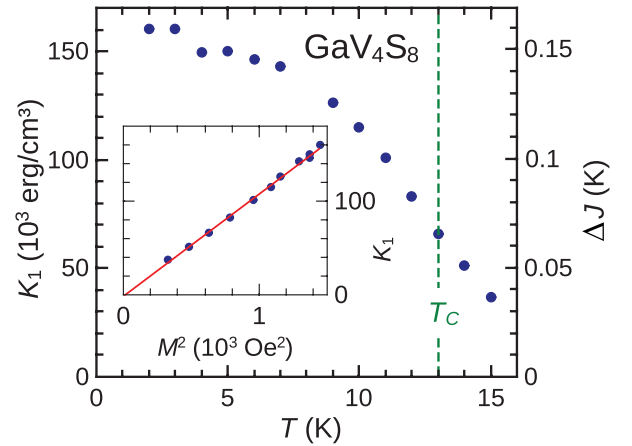

Figure 5. Temperature dependence of the first uniaxial anisotropy constant K_1 in GaV_4S_8, where the right scale expresses the corresponding exchange anisotropy ΔJ. The dashed line indicates the Curie temperature T_C. The inset shows K_1 as a function of the squared magnetization with a linear fit (solid line).

matches the Q-band data. We ascribe this splitting to distributions in the local strain, as discussed in section 3.1. Sample misalignment can be excluded as the sample was placed on the well-defined $(1\,1\,1)$ facet. Considering the Landé factor $g = 1.82$ given above and $K_1 = 1.2 \cdot 10^5\,\text{erg}\,\text{cm}^{-3}$, we simulate the resonance frequencies as seen as the turquoise solid lines, the upper one of which follows from (2). For $H \geqslant 1\,\text{kOe}$ they are in satisfying agreement with the field evolution of the resonance frequencies. This value of K_1 is 10% less than for the sample used in figure 5, but compares well with that one estimated for the sample employed in figure 3. Such a variation is common for samples from different batches having slight modifications of the sulphur content.

Another striking feature of the ESR dispersion ($T = 8\,\text{K}$) in figure 7 is the existence of two finite-frequency excitations at zero external field, a low-frequency excitation at 3.5 GHz and an (additionally split) high-frequency excitation at 20 GHz. The presence of two resonances has been reported earlier [25] and is characteristic of the cycloidal phase. The rather weak splitting of the high-frequency resonance suggests a heterogenous magnetic state at low fields, which has not been resolved until now.
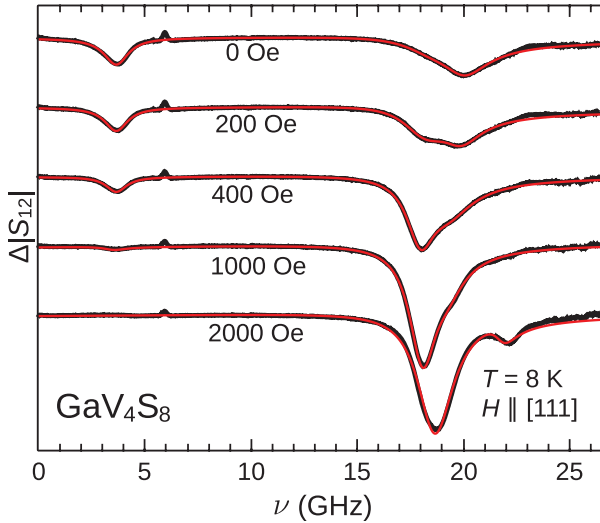
6

Figure 6. Frequency-swept ESR spectra (black) for a GaV_4S_8 single crystal with the external field applied along [1 1 1]. The spike at 6 GHz is an artefact. Data are fitted by a set of Lorentzian lines with antisymmetric contribution (red).
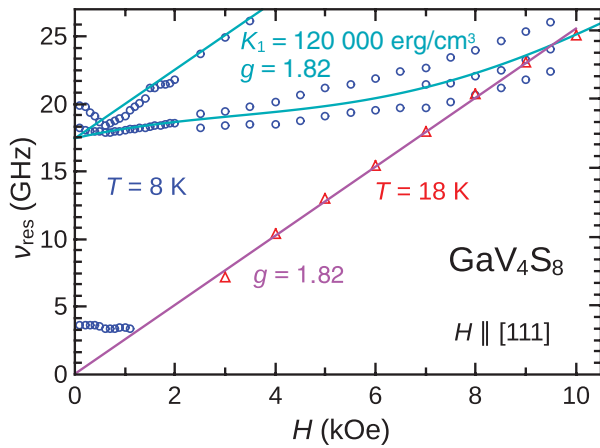

Figure 7. Resonance frequencies in GaV_4S_8 as a function of external field along [1 1 1]. Data from the ordered state (8 K, circles) and from the paramagnetic state (18 K, triangles) are shown. For the latter curve the violet line displays a linear regression, whereas the turquoise lines are simulations of ferromagnetic resonance.

4. Conclusion

Using ESR data we have determined the value of the magneto-crystalline anisotropy constant in GaV_4S_8 as a function of temperature. Corresponding to an anisotropy field at low temperatures in the order of 8 kOe, uniaxial anisotropy is the dominant magnetic interaction. This is a typical anisotropy for spinels, but an unusually large value as compared to other skyrmion hosts investigated so far. The sign of the magneto-crystalline anisotropy is positive, meaning easy-axis aniso-sotropy with axes parallel to the structural distortions along the $\langle 1\,1\,1 \rangle$ directions. The linear dependence of K_1 as function of the squared magnetization M^2 unravels the anisotropic exchange interaction as the source of magnetocrystalline anisotropy in GaV_4S_8.

While the spectral features above magnetic fields of 5 kOe are described as ferromagnetic resonances and these excitations merge towards low fields, a resonance at 3.5 GHz is characteristic of the data at low fields. It should be clarified by future work whether this resonance exists below 5 K, where, according to the currently accepted magnetic phase diagram of GaV_4S_8, no cycloidal spin structure is expected. Furthermore, the question of whether a single-domain state in GaV_4S_8 can be reached by application of uniaxial pressure remains a challenge.

References

[1] Abd-Elmeguid M M, Ni B, Khomskii D I, Pocha R, Johrendt D, Wang X and Syassen K 2004 *Phys. Rev. Lett.* **93** 126403
[2] Rastogi A K, Berton A, Chaussy J, Tournier R, Potel M, Chevrel R and Sergent M 1983 *J. Low Temp. Phys.* **52** 539–57
[3] Rastogi A K and Wohlfarth E P 1987 *Phys. Status Solidi* B **142** 569–73
[4] Vaju C, Cario L, Corraze B, Janod E, Dubost V, Cren T, Roditchev D, Braithwaite D and Chauvet O 2008 *Adv. Mater.* **20** 2760–5
[5] Cario L, Vaju C, Corraze B, Guiot V and Janod E 2010 *Adv. Mater.* **22** 5193–7
[6] Singh K, Simon C, Cannuccia E, Lepetit M B, Corraze B, Janod E and Cario L 2014 *Phys. Rev. Lett.* **113** 137602
[7] Pocha R, Johrendt D and Pöttgen R 2000 *Chem. Mater.* **12** 2882–7
[8] Nakamura H, Chudo H and Shiga M 2005 *J. Phys.: Condens. Matter* **17** 6015–24
[9] Bichler D, Zinth V, Johrendt D, Heyer O, Forthaus M K, Lorenz T and Abd-Elmeguid M M 2008 *Phys. Rev. B* **77** 212102
[10] Kézsmárki I *et al* 2015 *Nat. Mater.* **14** 1116
[11] Fert A, Cros V and Sampaio J 2013 *Nat. Nanotechnol.* **8** 152
[12] Mochizuki M, Yu X Z, Seki S, Kanazawa N, Koshibae W, Zang J, Mostovoy M, Tokura Y and Nagaosa N 2014 *Nat. Mater.* **13** 241
[13] Romming N, Kubetzka A and Hanneken C 2015 *Phys. Rev. Lett.* **114** 177203
[14] Bogdanov A and Hubert A 1994 *Phys. Status Solidi* B **186** 527
[15] Mühlbauer S, Binz B, Jonietz F, Pfleiderer C, Rosch A, Neubauer A, Georgii R and Böni P 2009 *Science* **323** 915
[16] Adams T *et al* 2011 *Phys. Rev. Lett.* **107** 217206
[17] Seki S, Yu X Z, Ishiwata S and Tokura Y 2012 *Science* **336** 198
[18] Seki S, Kim J H, Inosov D S, Georgii R, Keimer B, Ishiwata S and Tokura Y 2012 *Phys. Rev. B* **85** 220406

[19] Adams T, Chacon A, Wagner M, Bauer A, Brandl G, Pedersen B, Berger H, Lemmens P and Pfleiderer C 2012 *Phys. Rev. Lett.* **108** 237204
[20] Münzer W *et al* 2010 *Phys. Rev.* B **81** 041203
[21] Ruff E, Widmann S, Lunkenheimer P, Tsurkan V, Bordács S, Kézsmárki I and Loidl A 2015 *Sci. Adv.* **1** e1500916
[22] Wang Z, Ruff E, Schmidt M, Tsurkan V, Kézsmárki I, Lunkenheimer P and Loidl A 2015 *Phys. Rev. Lett.* **115** 207601
[23] Widmann S, Ruff E, Günther A, Krug von Nidda H A, Lunkenheimer P, Tsurkan V, Bordács S, Kézsmárki I and Loidl A 2016 *Philosophical Magazine* (doi: 10.1080/14786435.2016.1253885)
[24] Xu K and Xiang H J 2015 *Phys. Rev.* B **92** 121112
[25] Ehlers D, Stasinopoulos I, Tsurkan V, Krug von Nidda H A, Fehér T, Leonov A, Kézsmárki I, Grundler D and Loidl A 2016 *Phys. Rev.* B **94** 014406

[26] Nakamura H, Ikeno R, Motoyama G, Kohara T, Kajinami Y and Tabata Y 2009 *J. Phys.: Conf. Ser.* **145** 012077
[27] Schwarze T, Waizner J, Garst M, Bauer A, Stasinopoulos I, Berger H, Pfleiderer C and Grundler D 2015 *Nat. Mater.* **14** 478
[28] Skrotskii G V and Kurbatov L V 1965 Phenomenological theory of ferromagnetic resonance *Ferromagnetic Resonance* ed S V Vonsovskii (Oxford: Pergamon)
[29] Osborn J A 1945 *Phys. Rev.* **67** 351–7
[30] Tsurkan V, Mücksch M, Krug von Nidda H A, Hemberger J, Samusi D, Loidl A, Horn S and Tidecks R 2002 *Solid State Commun.* **123** 327–31
[31] Ehlers D, Tsurkan V, Krug von Nidda H A and Loidl A 2012 *Phys. Rev.* B **86** 174423
[32] Dyson F J 1955 *Phys. Rev.* **98** 349
[33] Barnes S E 1981 *Adv. Phys.* **30** 801